Selective phase filtering of charged beams with laser-driven antiresonant hollow-core fibers

L. Genovese,[1,*] M. Kellermeier,[1] F. Mayet,[1] K. Floettmann,[1] G. K. L. Wong,[2] M. H. Frosz,[2] R. Assmann,[1] P. St. J. Russell,[2] and F. Lemery[1,†]

[1]*Deutsches Elektronen-Synchrotron DESY, Notkestraße 85, 22607 Hamburg, Germany*

[2]*Max Planck Institute for the Science of Light, Staudtstraße 2, 91058 Erlangen, Germany*

(Received 28 July 2022; revised 20 December 2022; accepted 12 January 2023; published 10 February 2023)

Emerging accelerator concepts increasingly rely on the combination of high-frequency electromagnetic radiation with electron beams, enabling longitudinal phase space manipulation which supports a variety of advanced applications. The handshake between electron beams and radiation is conventionally provided by magnetic undulators which unfortunately require a balance between the electron beam energy, undulator parameters, and laser wavelength. Here we propose a scheme using laser-driven large-core antiresonant optical fibers to manipulate electron beams. We explore two general cases using TM_{01} and HE_{11} modes. In the former, we show that large energy modulations $O(100\ \text{keV})$. can be achieved while maintaining the overall electron beam quality. Further, we show that by using larger field strengths $O(100\ \text{MV/m})$ the resulting transverse forces can be exploited with beam-matching conditions to filter arbitrary phases from the modulated electron bunch, leading to the production of ≈100 attosecond FWHM microbunches. Finally, we also investigate the application of the transverse dipole HE_{11} mode and find it suitable for supporting time-resolved electron beam measurements with sub-attosecond resolution. We expect the findings to be widely appealing to high-charge pump-probe experiments, metrology, and accelerator science.

DOI: 10.1103/PhysRevResearch.5.013096

I. INTRODUCTION

Beyond the rigorously investigated static properties of matter, chemistry, and biology, the last decades have seen a large pursuit toward the development of time-resolved studies. Such pump-probe experiments are typically conducted under various and possibly extreme conditions and are paramount to the development of novel scientific theories and models which could enable future applications, technologies, and medicine.

In pump-probe experiments, a pump source (e.g., a high-intensity electromagnetic pulse) is used to excite a sample which is subsequently probed by, e.g., x-rays, electrons, or with a suitable electromagnetic pulse. The resulting sample response can be retrieved by varying the time separation between the pump and probe. State-of-the-art techniques based on high-harmonic generation (HHG) [1], electron diffraction (UED) and microscopy [2], or x-ray free-electron lasers (XFELs) [3] can now routinely reach femtosecond resolutions with available femtosecond-scale laser pulses, electron bunch lengths, and diagnostics.

Further extending our capacity to explore electronic motions which provide information on molecular dynamics at attosecond timescales has become highly sought after. While significant progress has been realized in HHG sources [4] and also in single-electron diffraction [5], there remain challenges in developing suitable tools to explore attosecond science in high-charge electron-based approaches, e.g., relativistic UED, microscopy, and XFELs. The development of novel techniques to produce and measure attosecond charged bunches could yield insightful information and provide means to develop ultrafast movies. Low-charge microbunched electron beams have also been widely discussed for their potential in electron microscopy [6–10].

Conventionally, laser-electron interactions are mediated with magnetic undulators [11]. The undulator imparts a transverse sinusoidal trajectory onto the electron beam which enables phase matching and energy transfer with the transversely polarized laser field. This technique has become ubiquitous in advanced accelerator science, enabling the development of laser heaters [12], FEL seeding schemes [13–16], and the compression and acceleration of electron beams [17,18]. However this approach has strict requirements on the undulator parameters for a given electron beam energy and laser wavelength which effectively limits the use of an undulator to a dedicated beam energy for a particular wavelength. This unfortunately leads to complex undulator designs at particularly low and high energies.

Alternatively, grating-style dielectric laser accelerators (DLAs) have recently been used to mediate laser-electron interactions [19–23]. Here however, structures are side-illuminated and rely on spatial harmonics that are evanescent across the accelerating channel, thereby limiting their apertures to approximately the laser wavelength to avoid nonlinear

*luca.genovese@desy.de
†francois.lemery@desy.de

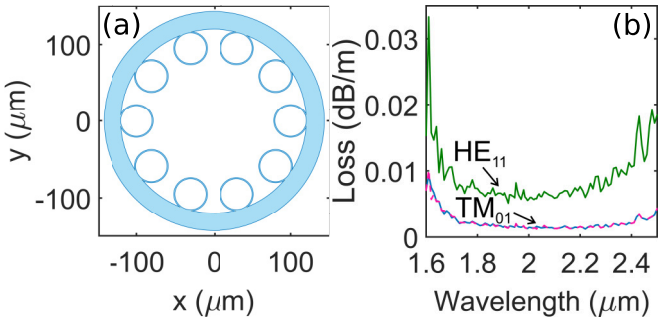

FIG. 1. Schematic of an ARF with an inner diameter D, supported by 10 AREs with wall thickness t and inner diameter d (a). The numerically calculated loss diagram for the TM_{01} and HE_{11} modes is shown in (b), illustrating the antiresonant low-loss bands.

fields which lead to beam quality degradation, e.g., emittance growth; this also limits the use case to very low charges, typically operating with single electrons per pulse. Moreover, mitigating beam losses in grating-DLAs requires the use of asymmetric beams with large transverse aspect ratios to enhance charge transmission through the small micrometer apertures. This restriction makes the widespread use of grating-DLAs in conventional relativistic electron beams produced by radio-frequency accelerators challenging, mainly due to typical round electron beam normalized emittances being $O(100\ \text{nm})$. The normalized emittance is a figure of merit defined as $\epsilon_u \equiv 1/(mc)[\langle u^2\rangle\langle p_u^2\rangle - \langle up_u\rangle^2]$, where m is the particle mass and c is the speed of light, along the transverse ($u = \perp$) and longitudinal ($u = z$) directions. DLAs in the form of cylindrical-symmetric photonic crystal fibers have also been investigated [24–27], yet no experimental demonstrations have been reported. Such cylindrical-symmetric accelerators could be advantageous, enabling the use of co-propagating TM_{01} modes used in conventional accelerators, providing means to more efficient acceleration with longer interaction distances while avoiding emittance growth. However, photonic crystal fibers with central core defects also have strict tolerances with respect to the injected laser wavelength, bandwidth, and mode shape to achieve synchronous acceleration. Fabrication of these fibers is also generally challenging due to the strict ratios between sizes of the core defect and surrounding channels. The development of dielectric laser accelerators with channel sizes comparable to the driving wavelength will likely require novel injectors and sources beyond radio-frequency-based technologies with picometer-level emittances. We note that another approach to energy-modulated single electrons in thin foils has also been realized [5]; however this scheme does not scale well to high-charge beams where foils generally lead to significant beam quality degradation. More recently, antiresonant photonic crystal fibers (ARFs) were invented [see Fig. 1(a)], which support low-loss transmission of enormously broadband spectra [28,29]. ARFs have relatively large apertures which relax the required electron beam parameters for efficient transmission through the fibers as has been routinely achieved in wakefield experiments at relatively high [30] and low energies [31]. In this article, we investigate the application of laser-driven ARFs with conventionally available electron beams produced with radio-frequency technology [32–34]. We especially find that high-quality energy modulations can be imparted with the monopole (TM_{01}) mode using μJ-level laser pulses. We further explore the use of mJ-level pulses with larger field strengths and discover that the large transverse forces can be exploited with beam-matching conditions to selectively filter phases of the modulated electron bunch with a collimator, creating attosecond microbunches. We also report on the use of the dipole (HE_{11}) mode and find it suitable to support sub-attosecond temporal measurement resolutions of charged beams. We expect our findings to have broad applications, especially in, e.g., high charge time resolved electron diffraction, microscopy, and accelerator science in general.

II. ANTIRESONANT FIBERS

Antiresonant fibers utilize a series of antiresonant elements (AREs) to confine radiation in a desired region. The simplest and most widely studied geometry of ARFs is the so-called revolver type [35]. Here as depicted in Fig. 1(a), ten capillaries are attached to the fiber cladding, and support the propagation of a largely broadband spectrum in the central core. The capillaries have appropriate dimensions to be resonant with the core mode, leading to large losses in the cladding [36–38] when

$$\lambda_q = \frac{2t}{q}\sqrt{n_g^2 - n_a^2}, \tag{1}$$

where t is the thickness of the capillaries, q is an integer which defines the order of the resonance, and n_g and n_a are the refractive indices of the capillaries and core, respectively. At wavelengths away from the resonances given by Eq. (1), however, the radiation is generally confined within the core with low losses. We note that ARFs are generally employed with applications in nonlinear optics where the core is filled with a gas with a particular pressure for the desired application [39]. In this study we reserve our investigations to a vacuum core, $n_a = 1$.

Compared to other types of hollow-core fibers, ARFs generally have lower overlap between the glass and the guided mode, leading to a higher damage threshold, which facilitates the propagation of mJ-level pulses. Loss factors have significantly improved in recent years due to novel designs and improved fabrication techniques, achieving 0.174 dB/km [40–42]. The loss coefficient is usually calculated numerically with finite-difference techniques; see Fig. 1(b) for an example of the calculated loss coefficient for the ARF waveguide considered in this work. Although ARFs with core diameters significantly larger than the antiresonant elements are inevitably multimode, with careful design of the launch optics it is possible to efficiently excite a selected mode.

Field descriptions were first discussed by Marcatili and Schmeltzer [43] in a simple case of hollow-core dielectric waveguides with infinite cladding based on a derivation from Stratton [44]. Modern analytical approaches describing fields in more complex, e.g., ring-type, ARFs rely on these general field formulations albeit with modified propagation constants [36]. We note that these derivations assume nonresonant conditions and a large core diameter compared to the wavelength

TABLE I. Hollow-core antiresonant fiber parameters.

description	symbol	value
hollow-core inner diameter	D	157 μm
number of capillaries		10
capillary inner diameter	d	40 μm
capillary wall thickness	t	1.5 μm
fused quartz refractive index	n	1.4373
$v_{ph}^{TM}/c-1$		1.15×10^{-4}
$v_{ph}^{HE}/c-1$		4.54×10^{-5}

($D \gg \lambda$), leading to propagation constants near free space ($k_z \approx k_0$).

We are particularly interested in the accelerating TM_{01} and fundamental deflecting HE_{11} modes which take the form

$$\mathrm{TM}_{01} = \begin{cases} E_r = ik_1k_zJ_1(k_1r), \\ E_z = k_1^2J_0(k_1r), \\ cB_\theta = ik_0k_1J_1(k_1r), \end{cases}$$

$$\mathrm{HE}_{11} = \begin{cases} E_r = i\left(k_z^2\frac{J_2(k_1r)}{k_1^2} + \frac{1}{r}\frac{J_1(k_1r)}{k_1}\right)\cos(\theta), \\ E_\theta = i\left(k_0^2\frac{J_2(k_1r)}{k_1^2} - \frac{1}{r}\frac{J_1(k_1r)}{k_1}\right)\sin(\theta), \\ E_z = k_0\frac{J_1(k_1r)}{k_1}\cos(\theta), \\ cB_r = -ik_0k_z\frac{J_2(k_1r)}{k_1^2}\sin(\theta), \\ cB_\theta = ik_0k_z\frac{J_2(k_1r)}{k_1^2}\cos(\theta), \\ cB_z = -k_0\frac{J_1(k_1r)}{k_1}\sin(\theta), \end{cases} \quad (2)$$

where ω is the angular frequency, $k_0 = 2\pi/\lambda = \omega/c$ is the wave number in free space, $k_z = \omega/v_{ph}$ is the propagation constant, v_{ph} is the phase velocity, J_m is the Bessel function of the first kind, θ is the angular coordinate, and $k_1 = \sqrt{k_0^2 - k_z^2}$; for brevity, the complex propagation phase $e^{i(\omega t - k_z z)}$ has been omitted from the equations. ARFs operating in vacuum support phase velocities beyond the speed of light ($v_{ph} > c$). We note that in the optics community, the effective refractive index is generally used and defined as $n_{\mathrm{eff}} = c/v_{ph}$ and is used interchangeably below.

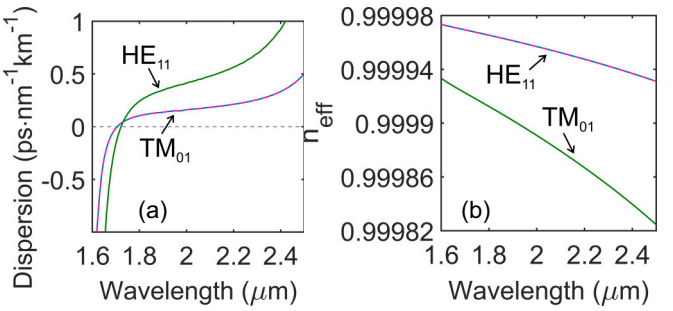

FIG. 3. The effective refractive index (n_{eff}) and dispersion are shown in (a) and (b), respectively, for the TM_{01} and HE_{11} modes.

In the remainder of the paper, we consider an ARF with parameters described in Table I. The same fiber supports both of the investigated modes. For completeness, the fields were also calculated with the wave optics module in COMSOL [45] using the finite-element method to solve Maxwell's equations in the frequency domain. The field maps for both the TM_{01} and HE_{11} modes are shown in Fig. 2 and are normalized to 1 W of input power. The signature of the AREs is especially noticeable in the longitudinal field components. The calculated fields are in good agreement with the analytical descriptions except in the vicinity of the AREs, where significant discrepancies in the fields appear. The difference between the calculated ($E_z^{(c)}$) and analytical ($E_z^{(a)}$) fields is estimated with the normalized integrated longitudinal field components within the core: $\int_0^{r=70\,\mu m} dr\frac{(E_z^{(a)}-E_z^{(c)})}{E_z^{(c)}} \sim 11\%$. Finally, in Fig. 3 we show the calculated n_{eff} and electromagnetic dispersion as a function of wavelength for both the TM_{01} and HE_{11} modes for a fiber with dimensions described in Table I.

The large core sizes of ARFs potentially enable their application with conventional charged particle beams with micron-level emittances. A primary limitation to electron beam interactions in ARFs is the distinction between massive particle velocities (v_e) being bound below the speed of light, in contrast to the phase velocities (v_{ph}) of modes in ARFs being bound beyond the speed of light. The interaction length before

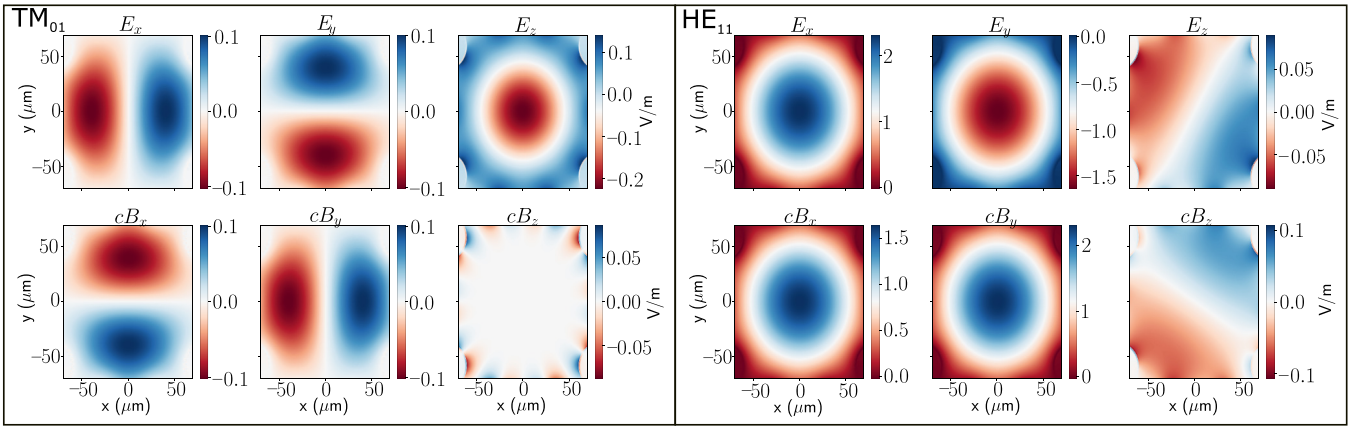

FIG. 2. Field maps for the TM_{01} (left) and HE_{11} (right) modes. The field maps were generated with COMSOL and imported to our particle-tracking simulations illustrated below. The antiresonant elements are especially noticeable in the outer portions of the longitudinal fields. We note that a smaller area of the ARF cross section is illustrated here compared to Fig. 1.

slipping by a half wavelength ($\lambda/2$) is given by

$$L < \frac{\lambda}{2\left(\frac{v_{ph}}{v_e} - 1\right)}. \tag{3}$$

However, as we discuss below, submillimeter-scale ARFs powered with sub-mJ pulses are sufficient to impart significant longitudinal and transverse momentum distributions in the ultrarelativistic regime.

The fields employed in our simulations were calculated with COMSOL [45] and imported directly into ASTRA [46] for beam dynamics simulations. Due to the relatively long simulation times required with space charge, we also compared results without space charge, to support the exploration of a large parameter space. We found negligible differences between simulations with and without space charge for the used 500 fC charges. Beam-loading effects are not considered in our work since no net energy is transferred via energy modulations. Similarly wakefields are anticipated to be negligible due to the weak coupling between the subluminal electron beam and the superluminal modes in the ARF.

Coupling into large aperture fibers with the fundamental HE_{11} (also known as the LP_{01}) is routine and yields typically near-unity coupling efficiencies by optimizing the beam size and divergence at the fiber entrance. Significant research has investigated coupling of vector modes, e.g., the TM_{01}. In this case, achieving high coupling efficiencies requires not only matching the beam at the fiber entrance, but also shaping the free-space mode to match the polarization distribution of the mode. This has previously been demonstrated by coherently combining [47] a segmented wave plate [48], or with a q plate [49]. In all studies, efficient coupling was achieved and mode excitations and qualities vary depending on the individual approach, but the TM_{01} is dominant. Alternative approaches using, e.g., spatial light modulators and other methods are also feasible.

III. ENERGY MODULATION WITH LASER-DRIVEN ARFs

The TM_{01} mode is the backbone of conventional radio-frequency accelerators (i.e., RF linacs), supporting a longitudinal accelerating field routinely used to increase beam energies. It is often desired to utilize a relatively small bunch length compared to the accelerating wavelength to minimize the energy spread of the accelerated beam. With micron-scale wavelengths however, this can be challenging to accomplish due to limitations in laser-RF synchronizations $O(10$ fs). To avoid synchronization difficulties, in this section we explore how an electron bunch with an rms bunch length of 20 fs and 100 MeV beam energy can interact with a TM_{01} mode driven by a 2 ps laser pulse with 2 μm wavelength; such a configuration is currently available at the ARES linac at DESY [50].

While RF linacs generally have insignificant RF focusing in the ultrarelativistic regime, the phase velocities supported by ARFs are larger than the speed of light, supporting azimuthally symmetric transverse forces. Here we investigate the utilization of a laser-driven TM_{01} mode with an electron bunch. As we show, with relatively low laser power, large energy modulations can be produced while maintaining the overall beam quality. In addition, we explore the utilization of large input laser powers, which leads to the development of coherent microbunches at the driving wavelength due to the periodic blowout of electrons from the large defocusing forces. After a 1 m drift we incorporate a collimator with a 700 μm diameter to remove the spoiled electrons. Moreover, we investigate how the final spectral content of the bunch can be modified with the inclusion of a weakly dispersive element; see Fig. 4 for an illustration of the complete scheme. The transverse forces within the ARF can be calculated with the Lorentz force, using the field approximations Eq. (2),

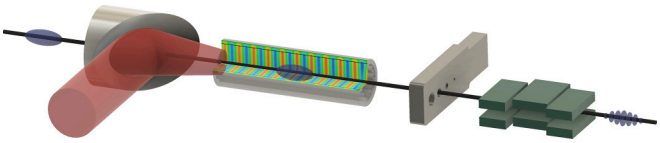

FIG. 4. Schematic of the microbunching setup. An electron beam passes through a laser-driven ARF with a length of 6 mm. The resulting laser excitation produces an energy modulation, and also strongly defocuses electrons periodically. The resulting defocused or spoiled electrons are absorbed on a collimator, producing a high-quality microbunched electron beam beyond the collimator. Finally, the addition of a weakly dispersive element can be used to further improve the form factor of the beam by converting the energy modulation into a density modulation.

$$F_r = ek_1k_0J_1(k_1r)(\beta - n_{\text{eff}})\sin(\Psi), \tag{4}$$

where $\Psi = \omega t - k_z z$ and β is the normalized beam velocity for the simulated 100 MeV electron beam. This results in the formation of focusing [$\Psi \in (0, \pi)$] and defocusing [$\Psi \in (\pi, 2\pi)$] forces along the bunch and also admits points with no transverse forces for $\Psi = 0$ and $\Psi = \pi$. In addition, there are additional transverse force contributions due to the radial coordinates of different particles due to $k_1 \neq 0$. We also note that the transverse force dependence is generally undesired since it leads to emittance growth; here we mitigate this effect by employing a relatively small beam size compared to the structure aperture.

By controlling the beam size and divergence into the fiber the final beam properties can vary greatly. We therefore first investigated how to efficiently match the electron beam into a relatively low-power laser-driven ARF by performing a parameter scan over the electron beam size (σ_r) and the correlated beam divergence (σ_r') at the entrance of the structure. Here we use the following initial electron beam parameters: $E = 100$ MeV, $Q = 500$ fC, $\epsilon_n = 50$ nm, $\sigma_t = 20$ fs, and a maximum on-axis longitudinal electric field of $E_z = 12$ MV/m (corresponding to an energy of ≈9 μJ). The resulting rms energy spread and final beam emittance are shown in Fig. 5. For a properly matched beam [e.g., $(\sigma, \sigma') = (5\ \mu\text{m}, -1.5\ \text{mrad})$] there is no emittance growth and the resulting energy modulation is smooth and sinusoidal. In this preliminary example, there is no collimator or dispersive section and the maximum peak-to-peak energy modulation is $E_{P2P} = 254$ keV, which is competitive with standard conventional undulator-based approaches used in, e.g., laser heaters at XFELs.

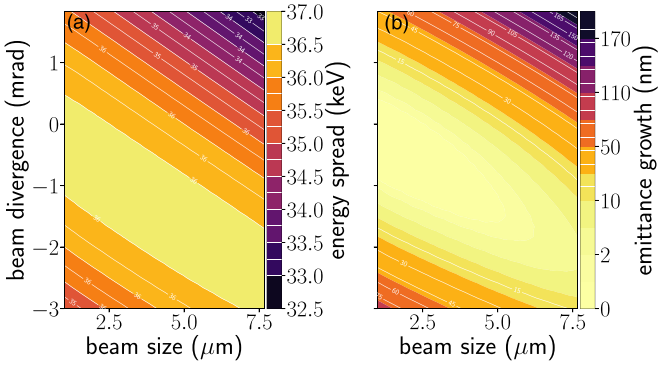

FIG. 5. Electron beam matching into a low-power [$E_z(r=0) \sim 12$ MV/m] laser-driven fiber with an excited TM_{01} mode in a 6 mm long ARF. The 2D parameter scan of the initial beam size at the structure entrance [$\sigma_r(z=0)$] and the correlated beam divergence (σ_r') is shown. The resulting energy spread and normalized emittance growth are displayed in (a) and (b), respectively.

IV. SELECTIVE PHASE FILTERING AND ATTOSECOND BUNCH TRAINS

The following discusses the beam dynamics associated with a high-power laser field near the damage threshold of the fiber, corresponding to $E_z = 180$ MV/m (and an input energy of 0.5 mJ; see [39] for information on damage thresholds in ARFs). In this scenario, the transverse forces are significant and dominate the beam dynamics, providing the opportunity to focus and defocus the beam strongly. However, due to the electron bunch being much longer than the wavelength, and due to phase slippage between the mismatched electron velocity and phase velocity, the integrated forces along the fiber are relevant; note the length of the fiber leads to approximately a phase slippage of a half wavelength. It is therefore appealing to introduce a collimator downstream of the ARF to filter out phases contributing to large beam sizes. In addition, by varying the beam size and divergence at the entrance of the ARF, it is possible to selectively filter different phases of the bunch, producing microbunched, or structured, beams. The resulting beam properties after the 700 μm diameter collimator located 1 m downstream of the ARF are displayed in Fig. 6. The strong transverse forces yield structured beams with enhanced bunch form factors for both converging or diverging beams (see below for a discussion on the bunch form factor). For converging beams (i.e., negative beam divergence), the periodic defocusing forces reduce the beam convergence, leading to larger transmission through the collimator for the integrated defocusing phases; note, however, that this leads to the destruction of the integrated focusing phases. Likewise for a diverging beam, the focusing forces reduce the divergence of the bunch periodically, also leading to larger local charge transmission through the collimator, but similarly leading to the destruction of the defocusing phases. Finally for collimated beams, i.e., no correlated divergence, the surviving phases correspond to regions of the bunch which have no integrated transverse forces. We note, by using a shorter ARF length, smaller phase regions could be preserved.

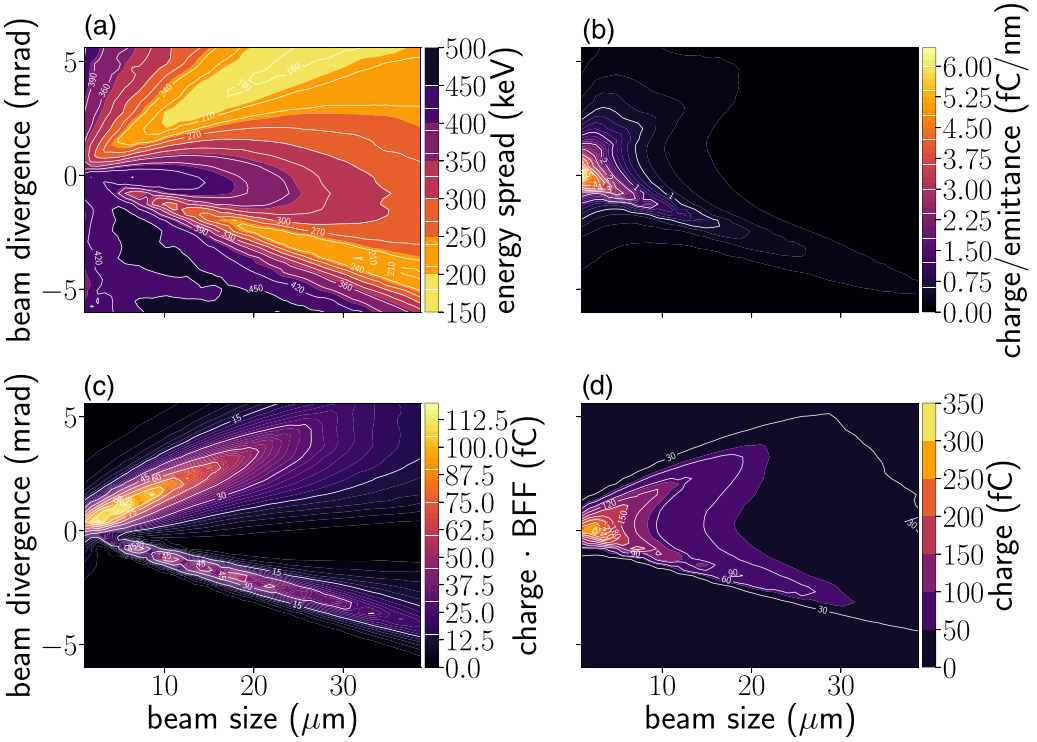

FIG. 6. Electron beam matching into a laser-driven fiber with an excited TM_{01} mode in a 6-mm-long ARF; the maximum on-axis accelerating field is $E_z = 180$ MV/m. The 2D parameter scan of the initial beam size at the structure entrance [$\sigma_r(z=0)$] and the correlated beam divergence (σ_r') is shown. The final beam properties after the collimator (placed 1 m downstream) are illustrated in the scans: energy spread (a), charge over normalized emittance (b), charge times the bunch form factor (c), and charge (d). Good matching regions are observed with large energy spreads, little emittance growth, and large charge transmission.

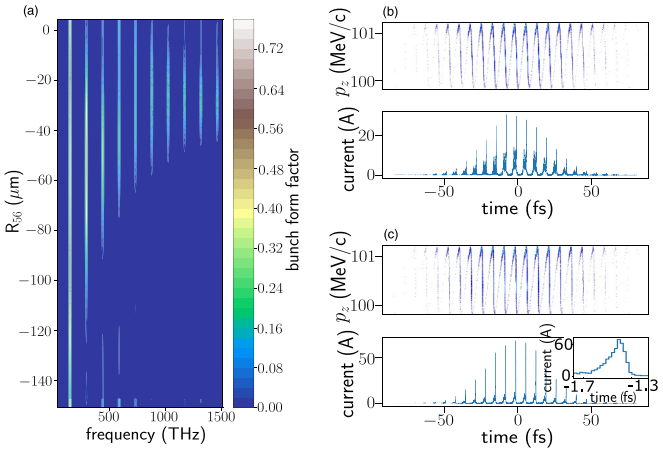

FIG. 7. The spectral range of the distribution achieved with matching parameters $(\sigma_r, \sigma_r') = (5\ \mu\text{m}, 0.5\ \text{mrad})$ is illustrated. Panel (a) shows the bunch form factor evolution as a function of the first-order momentum compaction R_{56}. Panel (b) provides an example of the resulting longitudinal phase space and current profile without any dispersive element ($R_{56} = 0$). We also display the resulting longitudinal phase space and current profile for the case of $R_{56} = -25\ \mu\text{m}$, corresponding to the case of maximum harmonic content in panel (c). Here the inset shows the microbunch with largest peak current which has a FWHM bunch duration of 140 as. Space charge forces are included in these results.

The results indicate that maintaining a low emittance beam requires the use of smaller beam sizes $\lesssim 5\ \mu\text{m}$.

Beyond the collimator, the beam is structured and has a significant correlated energy spread which can be converted to improve the density modulation. This is achieved by using a dispersive element which varies different particle path lengths based on their energies. A simple formula can be used to describe this transformation, $z_i \rightarrow z_f = z_i + R_{56}\delta$, where z_i and z_f are the initial and final particle positions, respectively, R_{56} is the first-order momentum compaction, and δ is the fractional energy spread. The necessary R_{56} required to achieve maximum compression in this scenario can be approximated with $R_{56} \approx \lambda/2\delta \approx -70\ \mu\text{m}$, where $\delta = E_{P2P}/E = 1.4\ \text{MeV}/100\ \text{MeV}$. The resulting spectral content of the bunch containing N macroparticles at a particular angular frequency ω can be calculated with the numerical bunch form factor of the macroparticle distribution,

$$F^2(\omega) = \frac{1}{N^2}\left(\left|\sum_{i=0}^{N}\cos\left(\frac{\omega z_i}{c}\right)\right|^2 + \left|\sum_{i=0}^{N}\sin\left(\frac{\omega z_i}{c}\right)\right|^2\right), \quad (5)$$

where z_i is the position of ith particle in the distribution.

In Fig. 7 we explore how dispersion influences the final spectral content of the distribution following the collimator with radius $r = 350\ \mu\text{m}$; the resulting form factor across a spectral range is shown in (a). Strong harmonic content extends to higher frequencies and is limited by the uncorrelated energy spread of the initial beam distribution. We provide an example of the longitudinal phase space and projected current profile of the distribution immediately after the collimator without dispersion in (b). The structured beam with large spectral content is a consequence of the periodically filtered portions of the bunch. Finally in (c), we show the resulting longitudinal phase space and projected current profile with $R_{56} = -25\ \mu\text{m}$, the setting with the largest spectral content. We note this final density modulation has microbunches with individual FWHM bunch lengths of approximately 140 as. In Table II, we describe the initial electron beam parameters (initial), the resulting beam parameters after the ARF (ARF) and the final collimated beam parameters (collimated).

V. LONGITUDINAL BUNCH DIAGNOSTICS AND METROLOGY WITH HE_{11}

In conventional accelerators, the hybrid dipole HE_{11} mode is routinely used for longitudinal bunch diagnostics, supporting the measurement of electron bunch lengths and longitudinal phase spaces when used with a spectrometer. The mode shears the beam by kicking the bunch head and tail in opposite transverse directions (e.g., up and down). After an appropriate drift following the kick, the resulting sheared electron bunch is imaged on a screen, providing the current profile.

The resolution of the streaking action is given by

$$R = \frac{\epsilon}{\sigma_y S} = \frac{\epsilon_n m_0 c^2}{\sigma_y e k V}, \quad (6)$$

where ϵ is the geometric emittance, ϵ_n is the normalized emittance ($\epsilon_n = \gamma\epsilon$), σ_y is the rms beam size in the ARF, S is the shearing parameter, m_0c^2 is the relativistic electron mass (0.511 MeV), $k = 2\pi/\lambda$ is the wave number of the driving field, and V is the maximum integrated voltage in the streaking plane. We note this equation relies on a phase advance in the transverse phase space of $\pi/2$ between the ARF and the imaging screen.

Achieving a high temporal resolution requires a large beam size compared to the driving wavelength which is naturally supported in ARFs. Here we explore the streaking performance of a laser-driven ARF. Similarly to the previous discussion, we first investigated proper matching through the ARF. Here however, due the relatively short bunch length used in our example ($\sigma_t = 1$ fs), the injection phase plays a significant role. We limit our investigation to injecting such that the phase slippage through the structure is symmetric through the zero crossing of the sinusoidal field by choosing the phase which leads to the bunch centroid staying on axis. We note that the resolution here is limited by the integrated voltage in the hollow core, which is in turn limited by phase slippage along the ARF and the field strength used. For a detailed discussion on beam dynamics in conventional transverse deflection structures including cases with phase slippage, see [51]. Presently, synchronization at this level is beyond the scope of conventional radio-frequency accelerators. However, by monitoring the beam position on a detector screen and sorting the resulting data, a useful measurement could be realized. Alternative laser-based acceleration techniques, e.g., plasma, dielectric laser, or DC accelerators, could possibly more easily incorporate this approach.

We now provide an example of the temporal resolution power of the ARF streaking mode. We consider a simple setup consisting of a 2-mm-long laser-driven ARF and a screen placed 50 cm downstream. The distance is sufficient to sup-

TABLE II. Electron beam parameters for microbunching.

parameter	initial	ARF	collimated
bunch length (σ_t) [fs]	20	20	20
transverse beam size ($\sigma_{x,y}$) [μm]	5	8.4	140
emittance ($\epsilon_{x,y}$) [nm]	50	970	140
average energy (E) [MeV]	100	100	100
peak-to-peak energy modulation (E_{P2P}) [MeV]		1.4	1.4
energy spread (dE) [keV]	20	442	368
charge [fC]	−500	−500	−162
ARF structure length (L) [mm]	6		
accelerating gradient [MV/m]	180		

port a phase advance of 80° which only limits the resolution by ∼1.5%. Here we use a modified electron bunch as in the previous discussion with the following initial parameters: $Q = 50$ fC, $\sigma_E = 20$ keV, $\epsilon_n = 50$ nm, $\sigma_r = 15$ μm, $\sigma_r' = 0$ mrad. In addition the example bunch is microbunched with a 10 attosecond periodicity; see Fig. 8. For these beam parameters and a field strength of 2 GV/m, the resolution power from Eq. (6) is ∼0.45 as. Beam-matching scans similar to the previous section can be found in [52] and show a large usable parameter space.

Finally, we show the resulting streaked beam 50 cm downstream of the ARF and the corresponding projected distribution in Fig. 8. Here the corresponding microbunch spacing on the screen is ≈170 μm. This powerful and relatively simple technique could be appealing for a multitude of applications, including high-charge pump-probe experiments, metrology, and XFEL optimizations.

VI. DISCUSSION

The rapid advancement of laser-based accelerators creates an exciting prospect for the next generation pump-probe experiments especially given the increasing interest in studying ultrafast attosecond phenomena. In this paper, we have proposed and explored the application of laser-driven antiresonant hollow-core fibers to support high-charge pump-probe experiments into the attosecond frontier. We have especially shown that the use of the TM_{01} mode could mediate energy transfer between lasers and electrons, enabling the energy modulation of electron beams on very compact footprints, in contrast to the relatively large and constrained undulator-based approaches. In a more extreme case where the laser power is increased, we also showed that the resulting transverse forces could produce microbunched beams at the driving wavelength and could further be improved by using a collimator to remove the spoiled electrons. Furthermore, by using a small dispersive element we showed that beams with a significant harmonic content could be produced.

We also reported on how the dipole HE_{11} mode could be employed as a bunch length diagnostic with sub-attosecond resolutions which is more than three orders of magnitude improvement on conventional radio-frequency-based methods. Such a powerful diagnostic could be invaluable in supporting emerging pump-probe experiments studying ultrafast processes, enabling detailed measurements.

The beam and laser parameters used here were chosen in relation to the available infrastructure at the ARES linac, DESY. We have also conducted simulations for lower (3.5 and 20 MeV) and higher (10 GeV) energies. Naturally larger interaction lengths are possible at higher energies. The strong relativistic velocity dependence at lower energies reduces the possible interaction lengths significantly. For example, considering the TM_{01} mode and beam energies of 20 and 5 MeV, maximum phase-matching lengths of 2.3 mm and 0.19 mm

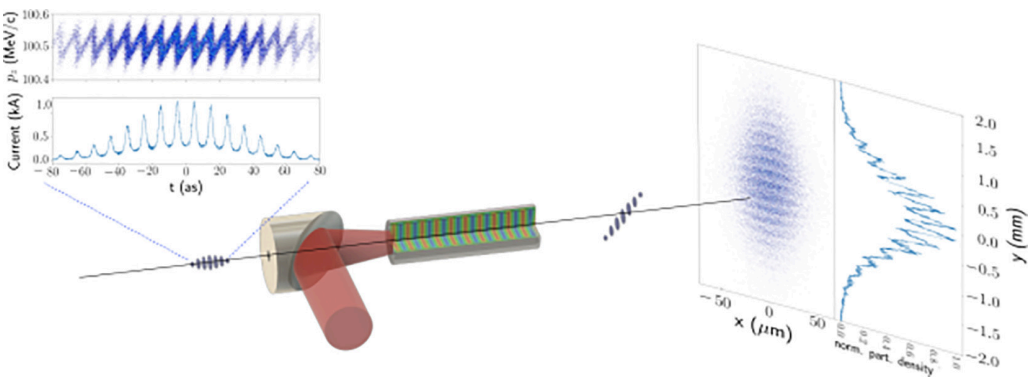

FIG. 8. An example of the streaking power of the HE_{11} mode. Here we consider an initial electron bunch with a 10 attosecond density modulation, with $Q = 50$ fC, $\sigma_r = 15$ μm, $\sigma_r' = 0$ mrad, $\epsilon_n = 50$ nm; see the initial LPS and projected current profile (top left). The electron bunch is then injected into the ARF with synchronized laser pulse. The streaking power of the ARF shears the bunch in the vertical plane onto a screen located 50 cm downstream of the ARF. The resulting transverse distribution and projection is displayed, illustrating the resolved 10 attosecond bunches.

could be reached, respectively, compared to a maximum interaction length of 8.9 mm in the ultrarelativistic limit. Larger energy modulations could be recovered by using femtosecond pulses with higher fields. For especially low energies it may be useful to conduct more elaborate simulations due to the limited structure length compared to wavelength. We note that the resolution of the transverse deflection discussion is energy independent.

We also expect this technique to appeal to accelerator science in general and could be complementary to radio-frequency-based accelerators. The large streaking powers could enable measurements of angstrom-level microbunches in XFELs, for example, but would require data sorting due to limitations in synchronization. Furthermore the simplicity of the scheme compared to undulator-based approaches could significantly simplify echo-enabled generation based light sources [13–15] and also proposed synthesizing techniques [16].

ACKNOWLEDGMENT

This project has received funding from the European Union's Horizon 2020 Research and Innovation program under Grant Agreement No. 730871.

[1] P. M. Paul, E. S. Toma, P. Breger, G. Mullot, F. Augé, P. Balcou, H. G. Muller, and P. Agostini, Observation of a train of attosecond pulses from high harmonic generation, Science **292**, 1689 (2001).

[2] D. Filippetto, P. Musumeci, R. Li, B. J. Siwick, M. Otto, M. Centurion, and J.P.F. Nunes, Ultrafast electron diffraction: Visualizing dynamic states of matter, Rev. Mod. Phys. **94**, 045004 (2022).

[3] D. E. Rivas, S. Serkez, T. M. Baumann, R. Boll, M. K. Czwalinna, S. Dold, A. de Fanis, N. Gerasimova, P. Grychtol, B. Lautenschlager, M. Lederer, T. Jezynksi, D. Kane, T. Mazza, J. Meier, J. Müller, F. Pallas, D. Rompotis, P. Schmidt, S. Schulz *et al.*, High-temporal-resolution x-ray spectroscopy with free-electron and optical lasers, Optica **9**, 429 (2022).

[4] N. Saito, H. Sannohe, N. Ishii, T. Kanai, N. Kosugi, Y. Wu, A. Chew, S. Han, Z. Chang, and J. Itatani, Real-time observation of electronic, vibrational, and rotational dynamics in nitric oxide with attosecond soft x-ray pulses at 400 eV, Optica **6**, 1542 (2019).

[5] Y. Morimoto and P. Baum, Diffraction and microscopy with attosecond electron pulse trains, Nat. Phys. **14**, 252 (2018).

[6] R. K. Li and P. Musumeci, Single-Shot MeV Transmission Electron Microscopy with Picosecond Temporal Resolution, Phys. Rev. Appl. **2**, 024003 (2014).

[7] P. Denham and P. Musumeci, Space-Charge Aberrations in Single-Shot Time-Resolved Transmission Electron Microscopy, Phys. Rev. Appl. **15**, 024050 (2021).

[8] D. Xiang, F. Fu, J. Zhang, X. Huang, L. Wang, X. Wang, and W. Wan, Accelerator-based single-shot ultrafast transmission electron microscope with picosecond temporal resolution and nanometer spatial resolution, Nucl. Instrum. Methods Phys. Res., Sect. A **759**, 74 (2014).

[9] S. V. Yalunin, A. Feist, and C. Ropers, Tailored high-contrast attosecond electron pulses for coherent excitation and scattering, Phys. Rev. Res. **3**, L032036 (2021).

[10] K. E. Priebe, C. Rathje, S. V. Yalunin, T. Hohage, A. Feist, S. Schäfer, and C. Ropers, Attosecond electron pulse trains and quantum state reconstruction in ultrafast transmission electron microscopy, Nat. Photonics **11**, 793 (2017).

[11] N. Kroll, P. Morton, and M. Rosenbluth, Free-electron lasers with variable parameter wigglers, IEEE J. Quantum Electron. **17**, 1436 (1981).

[12] E. Saldin, E. Schneidmiller, and M. Yurkov, Longitudinal space charge-driven microbunching instability in the TESLA Test Facility linac, Nucl. Instrum. Methods Phys. Res., Sect. A **528**, 355 (2004).

[13] G. Stupakov, Using the Beam-Echo Effect for Generation of Short-Wavelength Radiation, Phys. Rev. Lett. **102**, 074801 (2009).

[14] E. Hemsing, M. Dunning, B. Garcia, C. Hast, T. Raubenheimer, G. Stupakov, and D. Xiang, Echo-enabled harmonics up to the 75th order from precisely tailored electron beams, Nat. Photonics **10**, 512 (2016).

[15] P. Rebernik Ribič, A. Abrami, L. Badano, M. Bossi, H.-H. Braun, N. Bruchon, F. Capotondi, D. Castronovo, M. Cautero, P. Cinquegrana, M. Coreno, M. E. Couprie, I. Cudin, M. Boyanov Danailov, G. De Ninno, A. Demidovich, S. Di Mitri, B. Diviacco, W. M. Fawley, C. Feng *et al.*, Coherent soft x-ray pulses from an echo-enabled harmonic generation free-electron laser, Nat. Photonics **13**, 555 (2019).

[16] E. Hemsing and D. Xiang, Cascaded modulator-chicane modules for optical manipulation of relativistic electron beams, Phys. Rev. ST Accel. Beams **16**, 010706 (2013).

[17] N. Sudar, P. Musumeci, J. Duris, I. Gadjev, M. Polyanskiy, I. Pogorelsky, M. Fedurin, C. Swinson, K. Kusche, M. Babzien, and A. Gover, High Efficiency Energy Extraction from a Relativistic Electron Beam in a Strongly Tapered Undulator, Phys. Rev. Lett. **117**, 174801 (2016).

[18] N. Sudar, P. Musumeci, I. Gadjev, Y. Sakai, S. Fabbri, M. Polyanskiy, I. Pogorelsky, M. Fedurin, C. Swinson, K. Kusche, M. Babzien, and M. Palmer, Demonstration of Cascaded Modulator-Chicane Microbunching of a Relativistic Electron Beam, Phys. Rev. Lett. **120**, 114802 (2018).

[19] E. Peralta, K. Soong, R. J. England, E. R. Colby, Z. Wu, B. Montazeri, C. McGuinness, J. McNeur, K. J. Leedle, D. Walz, *et al.*, Demonstration of electron acceleration in a laser-driven dielectric microstructure, Nature (London) **503**, 91 (2013).

[20] J. Breuer and P. Hommelhoff, Laser-Based Acceleration of Nonrelativistic Electrons at a Dielectric Structure, Phys. Rev. Lett. **111**, 134803 (2013).

[21] D. Cesar, J. Maxson, X. Shen, K. P. Wootton, S. Tan, R. J. England, and P. Musumeci, Enhanced energy gain in a dielectric laser accelerator using a tilted pulse front laser, Opt. Express **26**, 29216 (2018).

[22] D. S. Black, U. Niedermayer, Y. Miao, Z. Zhao, O. Solgaard, R. L. Byer, and K. J. Leedle, Net Acceleration and Direct Measurement of Attosecond Electron Pulses in a Silicon Dielectric Laser Accelerator, Phys. Rev. Lett. **123**, 264802 (2019).

[23] N. Schönenberger, A. Mittelbach, P. Yousefi, J. McNeur, U. Niedermayer, and P. Hommelhoff, Generation and Characterization of Attosecond Microbunched Electron Pulse Trains via Dielectric Laser Acceleration, Phys. Rev. Lett. **123**, 264803 (2019).

[24] X. E. Lin, Photonic band gap fiber accelerator, Phys. Rev. ST Accel. Beams **4**, 051301 (2001).

[25] C.-K. Ng, R. J. England, L.-Q. Lee, R. Noble, V. Rawat, and J. Spencer, Transmission and radiation of an accelerating mode in a photonic band-gap fiber, Phys. Rev. ST Accel. Beams **13**, 121301 (2010).

[26] R. J. Noble, J. E. Spencer, and B. T. Kuhlmey, Hollow-core photonic band gap fibers for particle acceleration, Phys. Rev. ST Accel. Beams **14**, 121303 (2011).

[27] L. Genovese, R. Aßmann, U. Dorda, M. Kellermeier, W. Kuropka, F. Lemery, and F. Mayet, Tolerance studies and limitations for photonic bandgap fiber accelerators, in *10th International Particle Accelerator Conference, Melbourne (Australia), 19 May 2019–24 May 2019* (JACoW Publishing, Geneva, 2019), pp. 3605–3608.

[28] F. Benabid, J. C. Knight, G. Antonopoulos, and P. S. J. Russell, Stimulated raman scattering in hydrogen-filled hollow-core photonic crystal fiber, Science **298**, 399 (2002).

[29] C. Wei, R. J. Weiblen, C. R. Menyuk, and J. Hu, Negative curvature fibers, Adv. Opt. Photon. **9**, 504 (2017).

[30] S. Antipov, C. Jing, M. Fedurin, W. Gai, A. Kanareykin, K. Kusche, P. Schoessow, V. Yakimenko, and A. Zholents, Experimental Observation of Energy Modulation in Electron Beams Passing through Terahertz Dielectric Wakefield Structures, Phys. Rev. Lett. **108**, 144801 (2012).

[31] F. Lemery, P. Piot, G. Amatuni, P. Boonpornprasert, Y. Chen, J. Good, B. Grigoryan, M. Groß, M. Krasilinikov, O. Lishilin, G. Loisch, A. Oppelt, S. Philipp, H. Qian, Y. Renier, F. Stephan, and I. Zagorodnov, Passive Ballistic Microbunching of Nonultrarelativistic Electron Bunches Using Electromagnetic Wakefields in Dielectric-Lined Waveguides, Phys. Rev. Lett. **122**, 044801 (2019).

[32] M. Hachmann and K. Flöttmann, Measurement of ultra low transverse emittance at REGAE, Nucl. Instrum. Methods Phys. Res., Sect. A **829**, 318 (2016).

[33] J. Maxson, D. Cesar, G. Calmasini, A. Ody, P. Musumeci, and D. Alesini, Direct Measurement of Sub-10 fs Relativistic Electron Beams with Ultralow Emittance, Phys. Rev. Lett. **118**, 154802 (2017).

[34] C. J. R. Duncan, D. A. Muller, and J. M. Maxson, Lossless Monochromation for Electron Microscopy with Pulsed Photoemission Sources and Radio-Frequency Cavities, Phys. Rev. Appl. **14**, 014060 (2020).

[35] A. D. Pryamikov, A. S. Biriukov, A. F. Kosolapov, V. G. Plotnichenko, S. L. Semjonov, and E. M. Dianov, Demonstration of a waveguide regime for a silica hollow-core microstructured optical fiber with a negative curvature of the core boundary in the spectral region >3.5 μm, Opt. Express **19**, 1441 (2011).

[36] J. Archambault, R. Black, S. Lacroix, and J. Bures, Loss calculations for antiresonant waveguides, J. Lightwave Technol. **11**, 416 (1993).

[37] H. Stawska, M. Popenda, and E. Bereś-Pawlik, Anti-resonant hollow core fibers with modified shape of the core for the better optical performance in the visible spectral region-a numerical study, Polymers **10**, 899 (2018).

[38] M. Hou, F. Zhu, Y. Wang, Y. Wang, C. Liao, S. Liu, and P. Lu, Antiresonant reflecting guidance mechanism in hollow-core fiber for gas pressure sensing, Opt. Express **24**, 27890 (2016).

[39] P. Russell, P. Hölzer, W. Chang, A. Abdolvand, and J. Travers, Hollow-core photonic crystal fibres for gas-based nonlinear optics, Nat. Photonics **8**, 278 (2014).

[40] F. Yu, W. J. Wadsworth, and J. C. Knight, Low loss silica hollow core fibers for 3–4 μm spectral region, Opt. Express **20**, 11153 (2012).

[41] S.-f. Gao, Y.-y. Wang, W. Ding, D.-l. Jiang, S. Gu, X. Zhang, and P. Wang, Hollow-core conjoined-tube negative-curvature fibre with ultralow loss, Nat. Commun. **9**, 2828 (2018).

[42] G. T. Jasion, H. Sakr, J. R. Hayes, S. R. Sandoghchi, L. Hooper, E. N. Fokoua, A. Saljoghei, H. C. Mulvad, M. Alonso, A. Taranta, T. D. Bradley, I. A. Davidson, Y. Chen, D. J. Richardson, and F. Poletti, 0.174 dB/km hollow core double nested antiresonant nodeless fiber (DNANF), in *Optical Fiber Communication Conference (OFC) 2022* (Optica Publishing Group, 2022), p. Th4C.7.

[43] E. A. J. Marcatili and R. A. Schmeltzer, Hollow metallic and dielectric waveguides for long distance optical transmission and lasers, Bell Syst. Tech. J. **43**, 1783 (1964).

[44] J. A. Stratton, *Electromagnetic Theory* (John Wiley & Sons, Inc., 2015).

[45] COMSOL Multiphysics, https://www.comsol.com.

[46] K. Floettmann, A Space Charge Tracking Algorithm, https://www.desy.de/~mpyflo.

[47] A. A. Ishaaya, C. J. Hensley, B. Shim, S. Schrauth, K. W. Koch, and A. L. Gaeta, Highly-efficient coupling of linearly- and radially-polarized femtosecond pulses in hollow-core photonic band-gap fibers, Opt. Express **17**, 18630 (2009).

[48] S. Carbajo, E. Granados, D. Schimpf, A. Sell, K.-H. Hong, J. Moses, and F. X. Kärtner, Efficient generation of ultra-intense few-cycle radially polarized laser pulses, Opt. Lett. **39**, 2487 (2014).

[49] F. Kong, H. Larocque, E. Karimi, P. B. Corkum, and C. Zhang, Generating few-cycle radially polarized pulses, Optica **6**, 160 (2019).

[50] B. Marchetti, R. Assmann, R. Brinkmann, F. Burkart, U. Dorda, K. Floettmann, I. Hartl, W. Hillert, M. Huening, F. Jafarinia, S. Jaster-Merz, M. Kellermeier, W. Kuropka, F. Lemery, D. Marx, F. Mayet, E. Panofski, S. Pfeiffer, H. Schlarb, T. Vinatier *et al.*, SINBAD-ARES: A photo-injector for external injection experiments in novel accelerators at DESY, J. Phys.: Conf. Ser. **1596**, 012036 (2020).

[51] K. Floettmann and V. V. Paramonov, Beam dynamics in transverse deflecting rf structures, Phys. Rev. ST Accel. Beams **17**, 024001 (2014).

[52] L. Genovese, Laser-driven anti-resonant fibers: Acceleration and phase space manipulation of relativistic electron beams, Ph.D. thesis, University of Hamburg, 2022.